



OPEN

The Great Dimming of Betelgeuse seen by the Himawari-8 meteorological satellite

Daisuke Taniguchi¹✉, Kazuya Yamazaki² and Shinsuke Uno³

Betelgeuse, one of the most studied red supergiant stars^{1,2}, dimmed in the optical range by ~1.2 mag between late 2019 and early 2020, reaching a historical minimum^{3–5} called ‘the Great Dimming’. Thanks to enormous observational effort to date, two hypotheses remain that can explain the Dimming¹: a decrease in the effective temperature^{6,7} and an enhancement of the extinction caused by newly produced circumstellar dust^{8,9}. However, the lack of multiwavelength monitoring observations, especially in the mid-infrared, where emission from circumstellar dust can be detected, has prevented us from closely examining these hypotheses. Here we present 4.5 yr, 16-band photometry of Betelgeuse between 2017 and 2021 in the 0.45–13.5 μm wavelength range making use of images taken by the Himawari-8¹⁰ geostationary meteorological satellite. By examining the optical and near-infrared light curves, we show that both a decreased effective temperature and increased dust extinction may have contributed by almost equal amounts to the Great Dimming. Moreover, using the mid-infrared light curves, we find that the enhanced circumstellar extinction actually contributed to the Dimming. Thus, the Dimming event of Betelgeuse provides us with an opportunity to examine the mechanism responsible for the mass loss of red supergiants, which affects the fate of massive stars as supernovae¹¹.

Himawari-8 is a Japanese geostationary meteorological satellite orbiting 35,786 km above the equator at 140.7° E (ref. ¹⁰). Since 7 July 2015, Himawari-8 has taken images of the entire disk of the Earth once every 10 min using its optical and infrared imager, the Advanced Himawari Imager (AHI; Extended Data Fig. 1). The Himawari-8 satellite also observes the region of outer space around the edge of the Earth’s disk during every scan; this motivated us to develop a new concept: using meteorological satellites as ‘space telescopes’ for astronomy (Fig. 1).

One of the unique aspects of this concept of using Himawari-8 for astronomy is that it enables us to obtain high-cadence time series of mid-infrared images, which are hard to acquire with the usual astronomical instruments. Small ground-based telescopes can acquire time-series measurements¹², but the observations only cover wavelengths within the atmospheric window, and they are interrupted by the Sun for several months in most cases^{13,14}. In contrast, astronomical satellites and aircraft-carrying telescopes can observe stars in most wavelength ranges^{15–17}, but the observations require higher costs than ground-based telescopes. Survey telescopes orbiting the Earth for non-astronomical purposes—such as the Himawari-8 meteorological satellite—have the potential to overcome these problems. In this work, we demonstrate that the mystery of the Great Dimming of Betelgeuse can be solved with the aid of the time-series observations from Himawari-8, especially

those in the mid-infrared, with which the amount of dust around Betelgeuse can be determined.

Examining the images taken by the Himawari-8 satellite, we found that several bright stars, including Betelgeuse, sometimes appear in the images (Extended Data Fig. 2). We therefore measured the amount of light coming from Betelgeuse, typically once per 1.72 d, between January 2017 and June 2021, and we made a 4.5 yr catalogue of light curves in 16 bands covering 0.45–13.5 μm (Extended Data Fig. 3a). Comparing the light curves, that is, the time series of spectral energy distributions (SEDs), with a model SED for Betelgeuse, we determined the time variation of the main parameters of Betelgeuse, namely the radius R , effective temperature T_{eff} and extinction $A(V)$ in the optical range. In addition to these three parameters, which can be determined from optical or near-infrared observation^{8,18}, we also succeeded in determining the dust optical depth τ_{10} at 10 μm using our mid-infrared light curves. With this τ_{10} , we will examine the dust-production history around Betelgeuse.

Figure 2 shows the main results of this paper, namely, the time variations of the stellar parameters R , T_{eff} , $A(V)$ and τ_{10} together with the AB magnitudes for band 3 at 640 nm, which is located around the central part of the Johnson R band. From the time variations of R , T_{eff} and $A(V)$, we found that the Great Dimming of Betelgeuse, the drop of ~1.2 mag in the V magnitude⁴, is likely to be caused by a cooling of ~140 K in T_{eff} which results in a dimming of the V magnitude by ~0.6 mag, and an increase of ~0.6 mag in $A(V)$, which, by definition, darkens the V magnitude by ~0.6 mag. This result supports a previously suggested scenario in which the Dimming was caused by a combination of a decrease in T_{eff} and an increase in $A(V)$ (refs. ^{1,8}), although several shortcomings in our model SED should be kept in mind; some of the shortcomings are examined in Methods and Extended Data Fig. 4.

However, the cause of the enhanced $A(V)$ during the Great Dimming is still under debate. Several works have proposed that occultation by a newly formed circumstellar dust cloud might be a promising cause^{1,8}. In contrast to this dust-formation scenario, several other works have argued that the dust formation is unnecessary to explain the Dimming. For example, three-dimensional (3D) effects⁷ or molecular opacity^{19,20}, rather than dust extinction, can also explain the Dimming.

To examine whether or not the enhanced $A(V)$ during the Dimming is due to the circumstellar dust, we focus on the time variation of τ_{10} . Since τ_{10} was determined using the mid-infrared light curves of bands 12–14 at around 10 μm , where O-rich dust emissions dominate the flux^{21,22}, it reflects the amount of circumstellar dust that emits the infrared light. Therefore, using our infrared τ_{10} measurements, in contrast to optical diagnostics, we can directly trace the amount of circumstellar dust. Our measurements in Fig. 2e show an enhancement of τ_{10} during the Great Dimming, though

¹Department of Astronomy, School of Science, The University of Tokyo, Tokyo, Japan. ²Department of Earth and Planetary Science, School of Science, The University of Tokyo, Tokyo, Japan. ³Institute of Astronomy, School of Science, The University of Tokyo, Tokyo, Japan. ✉e-mail: d.taniguchi.astro@gmail.com

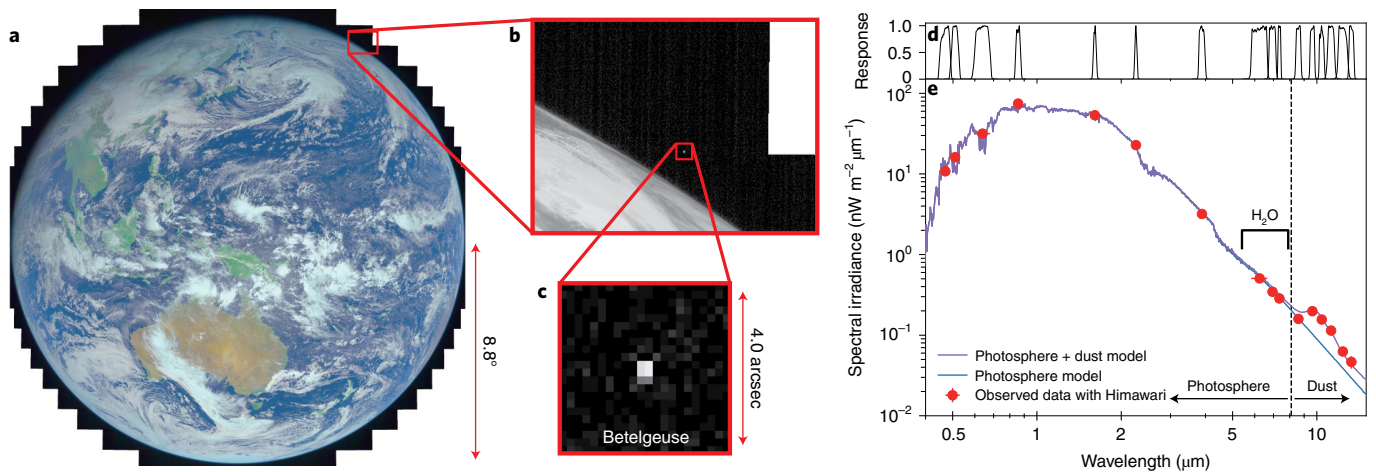


Fig. 1 | Betelgeuse observed with the Himawari-8 meteorological satellite near the edge of the Earth's disk. a, False-colour image taken by the Himawari-8 satellite on 19 January 2020. Betelgeuse is located at the top right corner of the image. **b, c**, Zoomed-in images of band 7. **d**, The response functions of Himawari-8; see the basic properties of the Himawari-8 data in Extended Data Fig. 1. **e**, The observed SED after averaging all observations with a model spectrum fitted to it.

there is a slight time delay between the peaks of $A(V)$ and τ_{10} . This enhancement of τ_{10} indicates that a clump of gas did in fact produce dust that shaded the photosphere of Betelgeuse and contributed to the Great Dimming.

Two potential dust reservoirs have been found so far for red supergiants. The first is a diffuse and spread-out dust layer located a few to several tens of stellar radii from the photosphere^{21,22}. In addition, instruments with very high spatial resolution have recently been used to find circumstellar dust clouds around red supergiants just a few tenths of a stellar radius above the photosphere^{23,24}. The distribution and amount of dust in the spread-out layer remain mostly unchanged with time^{22,25}, and thus it is unlikely that dust condensation in this layer is related to the large time variation of $A(V)$ and τ_{10} during the Dimming that we found. In contrast, the latter, lukewarm region²⁶ coexists with the warm chromosphere, the temperature of which^{9,27} is sufficiently high for dust sublimation²⁸. Therefore, a dust clump that condenses near the photosphere may soon be sublimated by chromospheric heating, or, if the radiative acceleration is insufficient, it may fall back to the photosphere to be sublimated²⁹. Considering these points, we conclude that the enhancements of $A(V)$ and τ_{10} during the Dimming may have occurred very close to the photosphere. This hypothesis is also supported by the fact that the polarized brightness of this circumstellar envelope changed substantially around the Dimming^{30,31}.

To further examine the dust-condensation process, we focus here on the time variation of the amount of molecular gas around Betelgeuse, in which the dust condensation occurred, and in particular on H_2O molecules. In addition to the dust emission seen at wavelengths around $10\mu m$, the number of molecules, particularly H_2O , can also be traced using Himawari-8 photometric data. Since H_2O molecules in the Earth's atmosphere absorb starlight³² in the wavelength ranges where the H_2O molecular features from stars exist³³, the observation of extraterrestrial H_2O molecules usually requires space telescopes¹⁵. One of the missions of the Himawari-8 satellite is to observe the distribution of water vapour in the Earth's upper atmosphere¹⁰, and thus Himawari-8 has the wavelength bands where H_2O features exist. These bands, bands 8–10 at around $6\text{--}8\mu m$, are therefore useful for time-series observations of H_2O molecules around Betelgeuse. We focus here on the flux variation of band 8, where the signal-to-noise ratio of the H_2O feature is maximized, thanks to the strength of this feature^{33,34} and the sensitivity of the Himawari-8 satellite (Extended Data Fig. 1). We note that the

$6\text{--}8\mu m$ wavelength range is a complicated region in which other molecular bands are present, for example, SiO molecules. Thus, we should keep in mind the possibility of contamination by these molecules, and further spectroscopic observations are required to fully disentangle the problem. Nevertheless, band 8 is the least contaminated by other molecules^{15,20,34}.

Figure 3 shows the time variation of the flux excess in band 8, defined as the ratio of the observed flux to predicted photospheric flux minus 1, which is likely to trace the amount of H_2O molecular gas around Betelgeuse, maybe in the MOLsphere^{15,34}. When gas clumps outside the photosphere are present that emit or absorb H_2O molecular features, the excess is positive or negative, respectively. In the first half of the observing period, that is, before September 2018, to within the error bars the flux excess was almost consistent with zero, which indicates that there was no extra detectable H_2O gas around the photosphere. In contrast, most of the data points after September 2018 show negative flux excesses. This indicates the emergence of a clump and/or a layer of cool gas containing H_2O molecules, in which the dust that dimmed Betelgeuse may have formed. Considering the clumpy nature of the dust cloud that dimmed Betelgeuse¹ and the existence of the warm gas clump found from ultraviolet observations of the $Mg\ II\ h$ and k lines around October 2019⁹, the H_2O gas that we found is also likely to be a clump.

Finally, and more interestingly, we tentatively identified a rapid transition in the H_2O feature from absorption to emission in early April 2019 (the green vertical line in Fig. 3). After visual inspection of the unbinned light curve for band 8, we found that the timescale of this transition is likely to be about a week or less. This timescale is much shorter than either the theoretical hydrodynamic timescale of a few weeks to a few months³⁵ or previously observed timescales of changes in the H_2O features seen in evolved red stars^{36,37}. Because the gas clump cannot move outside the line of sight to the photosphere on such a short timescale, this transition indicates the occurrence of an episodic bursty event. One may speculate that the cause of this unusual event is related to another rare event, the Great Dimming; if so, it would be easy to imagine that such an unusual event could occur. One conceivable scenario involves a shock wave passing through the clump. It has been suggested that such a shock emerged from the bottom of the photosphere in January 2019 and propagated from there to the outer envelope of Betelgeuse¹⁹. Together with the fact that $A(V)$ began to increase at the time of this transition (Fig. 2d), this shock might be related to the triggering

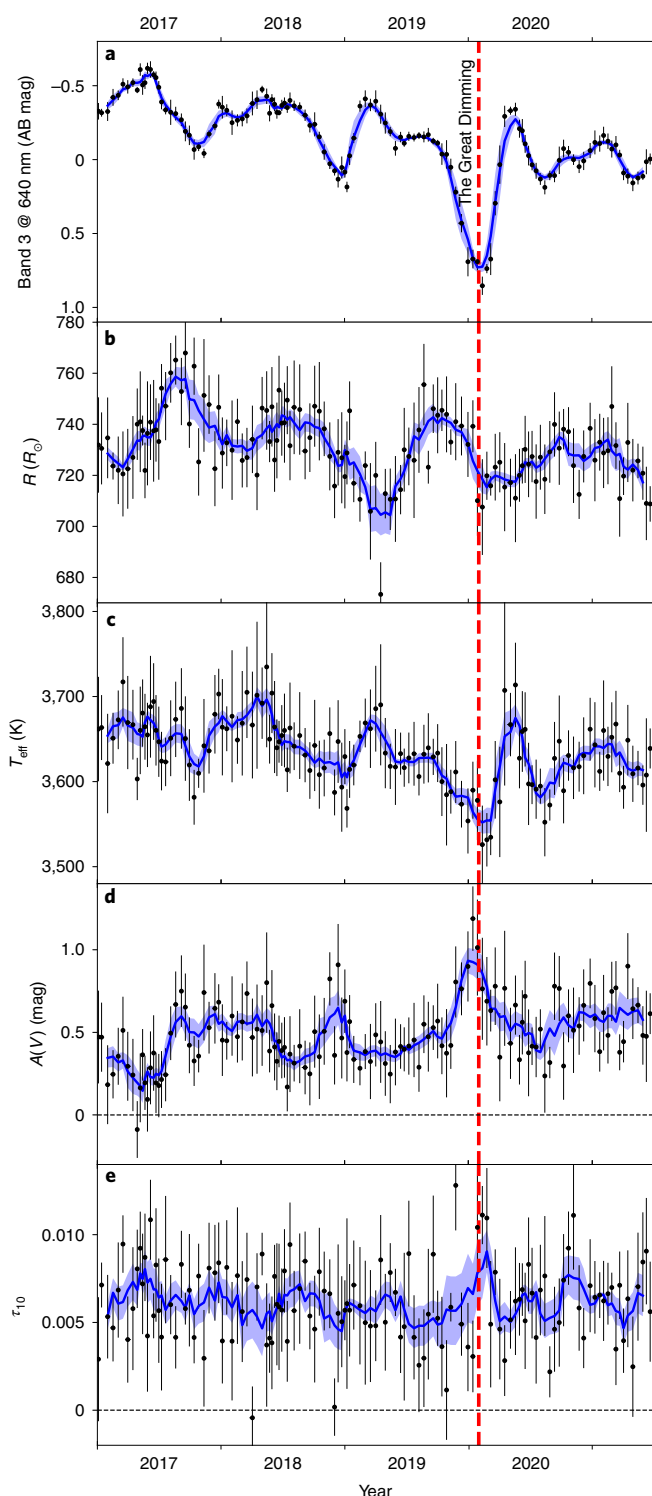


Fig. 2 | Time variation of the stellar parameters of Betelgeuse. The black dots with error bars represent the measured values and their s.e.m., and the blue lines and blue shading show versions smoothed by averaging five points to guide the eye and their s.e.m. **a**, The light curve of Betelgeuse at band 3, centred at 640 nm, in AB magnitudes. **b–e**, The results of the SED fitting. **b**, R . **c**, T_{eff} . **d**, $A(V)$. **e**, τ_{10} . The time of the Great Dimming is indicated by the red vertical line.

process of the Great Dimming. Future theoretical investigations and time series of spatially resolved infrared observations would enable us to tackle this further mystery.

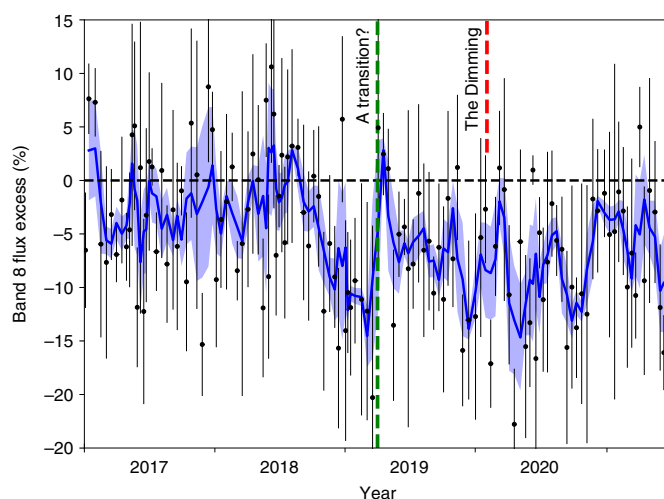


Fig. 3 | Molecular H_2O emission and absorption. The flux excess in band 8, where molecular H_2O features exist. The blue line and blue shading show a smoothed version and s.e.m. by averaging five points of the original black dots with error bars (measured values and s.e.m.) to guide the eye. We found a rapid transition in the flux excess from negative (absorption) to positive (emission) in early April 2019 (green vertical line), which occurs 10 months before the Great Dimming in early February 2020 (red vertical line).

Methods

We first aimed to establish and test a new concept, using meteorological satellites as astronomical space telescopes, to obtain multiband, long-term and continuous light curves uninterrupted by the Sun. Second, we applied this technique to Betelgeuse to investigate its mysterious Great Dimming.

Images of celestial objects, particularly the Moon, obtained by meteorological satellites have long been used only to calibrate and ensure the quality of Earth observations^{38–40}. In contrast, we attempted to use these images to investigate stellar astrophysics. Here, we thoroughly describe the data properties and the photometric methods and their validation.

Basic properties of the Himawari-8 scanning observation. Geostationary meteorological satellites, such as Himawari-8, observe the entire disk of the Earth by sequential scans with several rows, each of which is termed a swath^{10,41}. Each swath is scanned with a one-dimensional (1D)-like detector array from west to east. Due to this scanning procedure, the properties of images obtained by Himawari-8 have several differences compared with those obtained by typical astronomical observations using two-dimensional devices. Nevertheless, we can use the reduced and distributed data, termed the L1B product, as ordinary astronomical images, provided that several caveats are taken into consideration.

First, pixel navigation and data sampling are well controlled and regular, and their errors are usually smaller than 0.5 pix for Himawari-8⁴². Thus, we can precisely transform the position in the image onto its location in the sky.

Second, the fill factor of the pixels in the north–south direction is almost 100%, and the east–west sampling interval is smaller than the pixel size⁴¹. As such, we do not need to be concerned with undersampling due to gaps between pixels. Moreover, after the resampling process during the reduction described below, each image is transformed to the fixed square grid, which is very easy to use.

Third, because each row of unresampled images is observed by a single detector, inaccurate calibration of the detector occasionally introduces a stripe pattern into the obtained images. The strength of such a stripe has been shown to be small for observations of Earth scenes⁴³, but it has not yet been closely examined for faint sources such as stars. Therefore, it should be kept in mind that flux measurements of stars are possibly influenced by this relatively large systematic error.

Finally, other possibly minor effects include quantization noise, nonlinearity of the detector response, and frequency of the calibration. We will further examine some causes of systematic and/or statistical errors and validate the photometric results in Supplementary Discussion.

In this work, we limit our analyses to the images observed with the AHI on board the Himawari-8 satellite, which is a ‘third-generation meteorological satellite’ characterized by access to as many as 16 bands¹⁰. There also are three other third-generation satellites equipped with 16-band imagers: GOES-16 and GOES-17⁴⁴, which are operated by the National Aeronautics and Space

Administration and the National Oceanic and Atmospheric Administration, and GEO-KOMPSAT-2A⁴⁵, which is operated by the Korea Meteorological Administration. Although they have been operational since November 2016, March 2018 and July 2019, respectively, flux values outside the Earth's disk are found to be masked and unavailable in their published standard L1B products, which makes these data unusable for our analyses. Combined analyses with these satellites would improve the precision of our results, if their images of the space around the Earth's disk were to be made publicly available.

Reduction of the AHI images is performed by the Japan Meteorological Agency^{41,46}. This involves geometric regridding into a fixed coordinate system using a Lanczos-like resampling; a linear and global flux calibration using deep space as the background, with a solar diffuser for the optical and a blackbody for the infrared as standard flux sources; and nonlinear flux calibrations based on prelaunch ground tests. No corrections are made for atmospheric effects, nor is masking for cosmic rays performed.

Photometry of the Himawari-8 image. About 6 yr of 16-band images have been obtained by the Himawari-8 satellite at a frequency of once every 10 min. We restricted the scope of our analyses to data observed from January 2017 to June 2021 because systematic biases in the flux calibration and in the positioning were identified in observations from July 2015 to November 2016 (Supplementary Discussion). From this large number of images, we tried to find and measure the light from Betelgeuse, which is moving with the speed of the Earth's rotation, 15° h^{-1} , and which is found to be located in the field of view about once every two days. First, we calculated the times when Betelgeuse is in the direction of the Earth using the Astropy package⁴⁷, and we collected all the images in which Betelgeuse could be detected. Then we searched for the location of the Betelgeuse signal in each of these images in bands 1–10, where the signal-to-noise ratio (SNR) is high enough to detect the star. For each of these high-SNR bands, we searched for the location of the star by choosing the pixel with the largest counts among those pixels where Betelgeuse is expected to be located. In contrast, we inferred the locations in the other bands (bands 11–16) by shifting from the position of Betelgeuse in band 7, where the SNR is the highest, by around 30 arcsec depending upon the differences in the times of observation for the two bands.

The pixel scale of the published images in each band is larger than the actual radius of the point-spread function estimated from the radius of the telescope. Thus, the light from a point source occupies only $1 \times 1 \text{ pix}^2$ of the unreduced images, and it spreads out to $\sim 2 \times 2 \text{ pix}^2$ during the reduction process (Fig. 1a–c). Due to this small point-spread function radius, point-spread function photometry does not work well, so instead we used the aperture-photometry technique with a $7 \times 7 \text{ pix}^2$ square aperture. The background flux in the aperture was estimated and subtracted by fitting the flux within a square annulus around the star using a two-dimensional polynomial function. We set the inner width of the annulus to be 7 pix and the outer width to be 43, 21 and 21 pix for the bands with spatial resolutions of 0.5, 1.0 and 2.0 km, respectively. We selected these widths to minimize the impact of stripe-shaped fluctuations of the background. We selected the order of the polynomial to be in the range 0–4 for each measurement so that the Akaike information criterion calculated from the fitting residuals is minimized. Then, we estimated the stellar flux by summing the background-subtracted spectral irradiances within the $7 \times 7 \text{ pix}^2$ aperture.

Since the background shapes are not guaranteed to be continuously connected between adjacent swaths, we excluded from our analyses cases in which the $7 \times 7 \text{ pix}^2$ aperture spans multiple swaths. Furthermore, we trimmed the square annulus used for background estimation by requiring that the annulus does not span multiple swaths. Moreover, to avoid contamination from terrestrial light, we introduced distance thresholds from the edge of the Earth's disk (Extended Data Fig. 1).

Validation of the photometry. Here, we performed a wide variety of validation steps, not only with Betelgeuse but also with other bright stars located in the field of view of the Himawari-8 satellite (Extended Data Fig. 2). From the validation described in Supplementary Discussion and Supplementary Figs. 1–6, we found no evidence of any serious systematic bias in our photometry, and we thus conclude that the measurements are ready for further analyses. Nevertheless, it would be important, in a coming decade, to examine whether or not there are overlooked systematic effects in our method.

SED fitting to the Himawari-8 light curves. Figure 1d,e shows the SED averaged in time together with a model SED having the typical atmospheric parameters of Betelgeuse. The photometric bands with wavelengths of $\lesssim 8 \mu\text{m}$ (bands 1–10) are almost unaffected by the circumstellar dust emission, and thus they can be used to determine the atmospheric parameters of Betelgeuse. In contrast, the other bands receive radiation from silicate-dust emission at around $10 \mu\text{m}$, and they can thus be used to measure the amount of dust formed around Betelgeuse. We therefore first fitted the SED for bands 1–10 with a model photosphere for Betelgeuse to determine the photospheric parameters— R , T_{eff} and $A(V)$ —and we then determined τ_{10} using bands 12–14, which have the highest SNR for the dust emission. Five examples of the fitting results are shown in Extended Data Fig. 3b–f.

Our final time-series photometric catalogue of Betelgeuse is an incomplete one; the catalogue lacks fluxes in several bands on several observations.

This is especially serious for longer-wavelength bands, where the sky-background emission is stronger, and thus a larger number of photometric measurements was removed from the catalogue when the star was located near the edge of the Earth's disk. Moreover, the signal-to-noise ratios in the mid-infrared bands are typically small, ~ 1 . To deal with these difficulties, we binned each light curve over 5–12 observations, requiring that all the binned data points for bands 1–10 include five or more points. Note that the number of days in each bin is automatically determined by the observation frequency, which depends on the observation epoch. For example, there is a clump of observations in May–June 2018 with a frequency of 0.85 d, which leads to the smaller number of days in the bins. Finally, we calculated the resulting median and its standard error for each bin.

Model SED for the photosphere. We fitted each point of this 'complete' SED curve for bands 1–10 with a photospheric model SED using the LMFIT package⁴⁸. To obtain the model spectrum for the photosphere, we interpolated a grid of BT-NextGen model spectra⁴⁹ with solar metallicity and the surface gravity $\log g = 0.0$, assuming that this 1D model can be used to model the spectra of Betelgeuse in any phase. We used Cardelli's reddening law⁵⁰ with the selective-to-total extinction ratio $R_V = 3.1$ (ref. ⁵¹), assuming that this law can be extrapolated to longer wavelengths. We also used the parallax of 6.55 mas measured with the Hipparcos satellite⁵². Although the accuracy of the parallax of Betelgeuse is controversial^{53,54}, the choice of parallax value only changes the fitted radius in a relative way and does not affect the interpretation of the results. For the same reason, we do not take into account the error in the parallax value. The model spectra are then convolved with the response function of the AHI (September 2013 version retrieved from https://www.data.jma.go.jp/mscweb/en/himawari89/space_segment/spsg_ahi.html) to calculate the model SEDs for Betelgeuse, and we fitted the observed SED with the model.

Dependence on the model selection. For the grid of model spectra, we first tried the MARCS grid⁵⁵ with $15 M_\odot$ (refs. ^{54,56–59}), which is usually used to model the spectra of red supergiants^{51,60}. We found that the MARCS grid gives a smaller Akaike information criterion than the BT-NextGen grid, probably because the wavelengths and the strengths of the molecular bands in the MARCS grid are more accurate. Moreover, considering the fact that several previous works⁵¹ succeeded in reproducing observed optical spectra of red supergiants dominated by molecular TiO bands with MARCS models, MARCS models appear to be an appropriate grid for the synthesis of TiO bands in red supergiants. However, we found that the results of the fits obtained using the MARCS grid were physically unreasonable for most cases that we considered, for example, $A(V) < 0$ mag, although the reason, possibly related to 3D effects and/or circumstellar gas, is unclear. Thus, instead of the MARCS grid, we used the BT-NextGen grid to compute the model SED. Testing both the MARCS and NextGen grids, we found that the model parameters we obtained using the BT-NextGen grid vary with time in the same way as those obtained using the MARCS grid; that is, the differences between the time variations obtained using the two grids are roughly constant (Extended Data Fig. 4a–c). Therefore, the results of this paper using the NextGen grid are not affected quantitatively by the choice of model grid, as long as the time variations are interpreted in a relative way.

We have also tested whether or not other model assumptions affect the results. For example, a change in $\log g$ from 0.0 to -0.5 makes T_{eff} systematically ~ 80 K warmer and $A(V)$ systematically ~ 0.3 mag larger. Similarly, changing R_V from 3.1 to 4.4 (ref. ⁵¹) decreases T_{eff} by $\lesssim 10$ K and $A(V)$ by $\lesssim 0.05$ mag. From these tests, we concluded that, although the absolute values of R , T_{eff} and $A(V)$ depend on the model assumptions, their relative variations appear to have been determined to an accuracy of ~ 10 K in T_{eff} and ~ 0.05 dex in $A(V)$, both of which are much smaller than the fitting errors, ~ 40 K and ~ 0.2 dex, respectively.

3D effects in the photosphere. The temperatures that previous works^{8,19,61,62} and we have both derived assumed a 1D geometry for the model atmosphere. Thus these temperatures are affected by 3D effects in the optical spectrum of the real star⁷. In fact, the SED of a model with a given T_{eff} , especially the strength of the TiO molecular absorption bands that appear in the optical spectra of red supergiants⁸, has a variety of shapes due to 3D effects³⁵. Therefore, when we fit the observed SED of the real 3D photosphere of Betelgeuse with a 1D model SED, the fitted values of T_{eff} and $A(V)$ depend not only on T_{eff} and $A(V)$ themselves but also on the 3D effects³⁵. In particular, a time variation of the patchiness of the surface^{63,64} could affect the time variations of T_{eff} and $A(V)$ (ref. ⁷).

As a simplified test of the 3D effect on our fitting result, inspired by the optical image of Betelgeuse obtained during the Dimming^{1,25}, we considered a model photosphere composed of two regions with different T_{eff} , which is similar to the model used in a previous work⁷. In this model, we assume that the cooler part of the photosphere has a varying temperature and a varying area and that the warmer part has a fixed temperature of 3,650 K. In contrast to the previous model⁷, we are able to consider two additional free parameters, $A(V)$ and R ; without these two parameters we could not obtain a satisfactory fit to our multiwavelength data. Altogether, we considered four free parameters (R , $A(V)$ and the temperature and area fraction of the cooler part); for example, when the entire area of the photosphere is occupied by the cooler part, the fraction is 1.0. With this four-parameter model, due to the strong degeneracy between $A(V)$ and the area,

sometimes the fitting failed and gave unphysical results. To remove these cases, we excluded fitted results with areas greater than 1.0 or less than 0.0 as well as results for which the temperatures reached the boundaries of the acceptable range (we assumed 2,800 and 4,000 K for the lower and upper boundaries, respectively).

Extended Data Fig. 4d–g compare the fitted results obtained with the three-parameter model adopted in the main text and the four-parameter model described here. We found that with the four-parameter model the contribution of the increased $A(V)$ to the Dimming decreases but that it is still larger than zero (~ 0.4 mag). This result supports the robustness of our results in a qualitative sense. Since the four-parameter model examined here is too simple to take 3D effects fully into account⁷, future theoretical modelling with self-consistent hydrodynamic models⁶⁵ will be necessary.

Comparison with previous radial-velocity (RV) measurements. To check our SED fitting results, we compared the radius determined herein with previous RV measurements. Because the radius is given by the integration of the RV, we can validate the radius curve using literature RV curves.

First, we found time lags of up to ~ 80 d between the times of maximum brightness and minimum radius (Fig. 2). Although such a large lag was not expected in a simple 1D hydrodynamic model¹⁴, a lag between light and RV curves has been observationally found for Betelgeuse^{9,19,66}. Moreover, we found clockwise trajectories between the R/T_{eff} and band 3 flux for most observation periods (Extended Data Fig. 3h–o), which has been predicted theoretically^{54,67}. The exception, the relation between R and band 3 flux between 27 October 2017 and 24 December 2018 shown in Extended Data Fig. 3i, could be attributed to effects other than the fundamental-mode pulsation, such as the long secondary period⁶⁸; however, the actual cause remains unclear.

Second, we estimated the RV curve by calculating the differential of our radius curve, and compared it with literature RV curves^{19,66}. This comparison reveals an overall good agreement between our data and the results cited above, supporting the validity of our radius measurement, and hence other parameters. However, minor differences of up to $\sim 5 \text{ km s}^{-1}$ may exist, particularly in September 2018–November 2018 and September 2019–December 2019. Plausible causes of these differences are (1) our imperfect modelling of Himawari-8's SEDs with a 1D model atmosphere, as discussed in the previous subsection, and (2) differences in the atmospheric layers that were observed in the present and previous studies, and hence the real, physical difference in RVs¹⁹.

Model SED for the dust emission. After fitting the SED curve for bands 1–10, we calculated the expected photospheric flux curves for bands 11–16 and subtracted them from the observed flux curves. These residual fluxes are likely to originate from the circumstellar dust emission, and they are useful for estimating the variation of the amount of circumstellar dust.

For the model spectra of the circumstellar dust emission, we used the radiative-transfer code DUSTY V2⁶⁹. For the settings of the DUSTY calculation, we basically followed the procedure described in a previous work⁷⁰, except for several modifications. First, we only fitted τ_{10} and fixed the other parameters. We used the ‘warm silicates’ dust composition⁷¹, a constant grain size of $0.3 \mu\text{m}$ and a constant dust temperature of 1,300 K at the inner boundary, which roughly corresponds to the sublimation temperature of silicate dust²⁸. Although inner-boundary temperatures less than 1,300 K are sometimes found using observations of red supergiants⁷⁰, we adopted this value since a different inner-boundary temperature only results in a systematic bias in τ_{10} as long as the temperature is independent of time. We also tried the assumption of a constant radius at the inner boundary, and we found that the results do not change in a qualitative sense. For the stellar radiation that illuminates the dust, we used the time variation of T_{eff} determined in the previous section to calculate the natal photospheric SED, after applying spline smoothing to reduce the noise in each measurement. Then, we calculated the expected silicate-dust emission in bands 12–14 on the τ_{10} grid and determined the τ_{10} value that best matches the observed flux-residual curve for each of bands 12–14. Finally, we calculated the mean of the three τ_{10} values determined from bands 12–14 to obtain the final estimate of τ_{10} . We note that the τ_{10} that we determined is in fact not the actual optical depth at $10 \mu\text{m}$; it is rather a model parameter that we use to match the observed and model fluxes of bands 12–14, and we use it as an indicator of the amount of circumstellar silicate around Betelgeuse.

Data availability

Reduced images taken by the Himawari-8 satellite are publicly available at the Data Integration and Analysis System via <https://diasjp.net/en/>. The final photometric product of this paper is available at https://d-taniguchi-astro.github.io/homepage/Data_Himawari_en.html, which is archived as Supplementary Data.

Code availability

We used the LMFIT package⁴⁸ to fit the observed SED in the optical to near infrared range with publicly available NextGen⁴⁹ and MARCS⁵⁵ model grids. We also used the DUSTY V2 code⁶⁹ to calculate the dust emission. We have not made the codes for the photometry publicly available because they are not prepared for open use. Instead, we have made the photometric catalogue available, as described in the data availability statement.

Received: 10 December 2021; Accepted: 11 April 2022;
Published online: 30 May 2022

References

- Montargès, M. et al. A dusty veil shading Betelgeuse during its Great Dimming. *Nature* **594**, 365–368 (2021).
- Ohnaka, K. et al. Imaging the dynamical atmosphere of the red supergiant Betelgeuse in the CO first overtone lines with VLT/AMBER. *Astron. Astrophys.* **529**, A163 (2011).
- Guinan, E. F., Wasatonic, R. J. & Calderwood, T. J. The fainting of the nearby red supergiant Betelgeuse. *The Astronomer's Telegram* **13341** (2019).
- Guinan, E., Wasatonic, R., Calderwood, T. & Carona, D. The fall and rise in brightness of Betelgeuse. *The Astronomer's Telegram* **13512** (2020).
- Sigismundi, C. Rapid rising of Betelgeuse's luminosity. *The Astronomer's Telegram* **13601** (2020).
- Dharmawardena, T. E. et al. Betelgeuse fainter in the submillimeter too: an analysis of JCMT and APEX monitoring during the recent optical minimum. *Astrophys. J. Lett.* **897**, L9 (2020).
- Harper, G. M., Guinan, E. F., Wasatonic, R. & Ryde, N. The photospheric temperatures of Betelgeuse during the Great Dimming of 2019/2020: no new dust required. *Astrophys. J.* **905**, 34 (2020).
- Levesque, E. M. & Massey, P. Betelgeuse just is not that cool: effective temperature alone cannot explain the recent dimming of Betelgeuse. *Astrophys. J. Lett.* **891**, L37 (2020).
- Dupree, A. K. et al. Spatially resolved ultraviolet spectroscopy of the Great Dimming of Betelgeuse. *Astrophys. J.* **899**, 68 (2020).
- Bessho, K. et al. An introduction to Himawari-8/9—Japan's new-generation geostationary meteorological satellites. *J. Meteorol. Soc. Jpn* **94**, 151–183 (2016).
- Beasor, E. R., Davies, B. & Smith, N. The impact of realistic red supergiant mass loss on stellar evolution. *Astrophys. J.* **922**, 55 (2021).
- Gehr, R. D. et al. Betelgeuse remains steadfast in the infrared. *The Astronomer's Telegram* **13518** (2020).
- Dupree, A., Guinan, E., Thompson, W. T. & STEREO/SECCHI/HI Consortium. Photometry of Betelgeuse with the STEREO mission while in the glare of the Sun from Earth. *The Astronomer's Telegram* **13901** (2020).
- Nickel, O. & Calderwood, T. Daylight photometry of bright stars—observations of Betelgeuse at solar conjunction. *J. Am. Assoc. Var. Star Obs.* **49**, 269 (2021).
- Tsuji, T. Water in emission in the Infrared Space Observatory spectrum of the early M supergiant star μ Cephei. *Astrophys. J. Lett.* **540**, L99–L102 (2000).
- Harper, G. M. et al. SOFIA-EXES observations of Betelgeuse during the Great Dimming of 2019/2020. *Astrophys. J. Lett.* **893**, L23 (2020).
- Harper, G. M. et al. SOFIA upGREAT/FIFI-LS emission-line observations of Betelgeuse during the Great Dimming of 2019/2020. *Astron. J.* **162**, 246 (2021).
- Taniguchi, D. et al. Effective temperatures of red supergiants estimated from line-depth ratios of iron lines in the YJ bands, $0.97\text{--}1.32 \mu\text{m}$. *Mon. Not. R. Astron. Soc.* **502**, 4210–4226 (2021).
- Kravchenko, K. et al. Atmosphere of Betelgeuse before and during the Great Dimming event revealed by tomography. *Astron. Astrophys.* **650**, L17 (2021).
- Davies, B. & Plez, B. The impact of winds on the spectral appearance of red supergiants. *Mon. Not. R. Astron. Soc.* **508**, 5757–5765 (2021).
- Verhoelst, T. et al. Amorphous alumina in the extended atmosphere of α Orionis. *Astron. Astrophys.* **447**, 311–324 (2006).
- Kervella, P. et al. The close circumstellar environment of Betelgeuse. II. Diffraction-limited spectro-imaging from 7.76 to $19.50 \mu\text{m}$ with VLT/VISIR. *Astron. Astrophys.* **531**, A117 (2011).
- Haubois, X. et al. The inner dust shell of Betelgeuse detected by polarimetric aperture-masking interferometry. *Astron. Astrophys.* **628**, A101 (2019).
- Asaki, Y. et al. ALMA high-frequency long baseline campaign in 2017: band-to-band phase referencing in submillimeter waves. *Astrophys. J. Suppl.* **247**, 23 (2020).
- Montargès, M. et al. ESO telescope sees surface of dim Betelgeuse. *ESO Press Release ESO2003* <https://www.eso.org/public/news/eso2003/> (2020).
- Ohnaka, K. et al. High spectral resolution imaging of the dynamical atmosphere of the red supergiant Antares in the CO first overtone lines with VLT/AMBER. *Astron. Astrophys.* **555**, A24 (2013).
- O'Gorman, E. et al. ALMA and VLA reveal the lukewarm chromospheres of the nearby red supergiants Antares and Betelgeuse. *Astron. Astrophys.* **638**, A65 (2020).
- Gupta, A. & Sahijpal, S. Thermodynamics of dust condensation around the dimming Betelgeuse. *Mon. Not. R. Astron. Soc.* **496**, L122–L126 (2020).
- Cannon, E. et al. The inner circumstellar dust of the red supergiant Antares as seen with VLT/SPHERE/ZIMPOL. *Mon. Not. R. Astron. Soc.* **502**, 369–382 (2021).
- Cotton, D. V., Bailey, J., De Horta, A. Y., Norris, B. R. M. & Lomax, J. R. Multi-band aperture polarimetry of Betelgeuse during the 2019–20 Dimming. *Res. Not. Am. Astron. Soc.* **4**, 39 (2020).

31. Safonov, B. et al. Differential speckle polarimetry of Betelgeuse in 2019–2020: the rise is different from the fall. Preprint at <https://arxiv.org/abs/2005.05215> (2020).
32. Shaw, J. A. & Nugent, P. W. Physics principles in radiometric infrared imaging of clouds in the atmosphere. *Eur. J. Phys.* **34**, S111 (2013).
33. Polyansky, O. L. et al. ExoMol molecular line lists XXX: a complete high-accuracy line list for water. *Mon. Not. R. Astron. Soc.* **480**, 2597–2608 (2018).
34. Perrin, G. et al. The molecular and dusty composition of Betelgeuse's inner circumstellar environment. *Astron. Astrophys.* **474**, 599–608 (2007).
35. Chiavassa, A., Freytag, B., Masseron, T. & Plez, B. Radiative hydrodynamics simulations of red supergiant stars. IV. Gray versus non-gray opacities. *Astron. Astrophys.* **535**, A22 (2011).
36. Matsuura, M., Yamamura, I., Cami, J., Onaka, T. & Murakami, H. The time variation in infrared water-vapour bands in Mira variables. *Astron. Astrophys.* **383**, 972–986 (2002).
37. Gravity Collaboration et al. MOLsphere and pulsations of the Galactic Center's red supergiant GCIRS 7 from VLTI/GRAVITY. *Astron. Astrophys.* **651**, A37 (2021).
38. Kieffer, H. H. Photometric stability of the lunar surface. *Icarus* **130**, 323–327 (1997).
39. Fulbright, J. P. & Xiong, X. Suomi-NPP VIIRS day/night band calibration with stars. *Proc. SPIE* **9607**, 96071S (2015).
40. Stone, T. C., Kieffer, H., Lukashin, C. & Turpie, K. The Moon as a climate-quality radiometric calibration reference. *Remote Sens.* **12**, 1837 (2020).
41. Kalluri, S. et al. From photons to pixels: processing data from the Advanced Baseline Imager. *Remote Sens.* **10**, 177 (2018).
42. Tabata, T. et al. Himawari-8/AHI latest performance of navigation and calibration. *Proc. SPIE* **9881**, 98812J (2016).
43. Gunshor, M. M., Schmit, T. J., Pogorzala, D., Lindstrom, S. & Nelson, J. P. GOES-R series ABI imagery artifacts. *J. Appl. Remote Sens.* **14**, 032411 (2020).
44. Schmit, T. J. et al. Introducing the next-generation Advanced Baseline Imager on GOES-R. *Bull. Am. Meteorol. Soc.* **86**, 1079–1096 (2005).
45. Kim, D., Gu, M., Oh, T.-H., Kim, E.-K. & Yang, H.-J. Introduction of the Advanced Meteorological Imager of Geo-Kompsat-2A: in-orbit tests and performance validation. *Remote Sens.* **13**, 1303 (2021).
46. Yokota, H. & Sasaki, M. Introduction to Himawari-8 and 9. *Meteorol. Satell. Cent. Tech. Note* **58**, 121–138 (2013).
47. Astropy Collaboration et al. Astropy: a community Python package for astronomy. *Astron. Astrophys.* **558**, A33 (2013).
48. Newville, M., Stensitzki, T., Allen, D. B. & Ingargiola, A. LMFIT: Non-Linear Least-Square Minimization and Curve-Fitting for Python (2014). <https://zenodo.org/record/11813#.YnDQLNrP02w>
49. Allard, F., Homeier, D. & Freytag, B. Models of very-low-mass stars, brown dwarfs and exoplanets. *Phil. Trans. R. Soc. A* **370**, 2765–2777 (2012).
50. Cardelli, J. A., Clayton, G. C. & Mathis, J. S. The relationship between infrared, optical, and ultraviolet extinction. *Astrophys. J.* **345**, 245–256 (1989).
51. Levesque, E. M. et al. The effective temperature scale of Galactic red supergiants: cool, but not as cool as we thought. *Astrophys. J.* **628**, 973–985 (2005).
52. van Leeuwen, F. Validation of the new Hipparcos reduction. *Astron. Astrophys.* **474**, 653–664 (2007).
53. Harper, G. M. et al. An updated 2017 astrometric solution for Betelgeuse. *Astron. J.* **154**, 11 (2017).
54. Joyce, M. et al. Standing on the shoulders of giants: new mass and distance estimates for Betelgeuse through combined evolutionary, asteroseismic, and hydrodynamic simulations with MESA. *Astrophys. J.* **902**, 63 (2020).
55. Gustafsson, B. et al. A grid of MARCS model atmospheres for late-type stars. I. Methods and general properties. *Astron. Astrophys.* **486**, 951–970 (2008).
56. Ekström, S. et al. Grids of stellar models with rotation. I. Models from 0.8 to 120 M_{\odot} at solar metallicity ($Z=0.014$). *Astron. Astrophys.* **537**, A146 (2012).
57. Dolan, M. M. et al. Evolutionary tracks for Betelgeuse. *Astrophys. J.* **819**, 7 (2016).
58. Wheeler, J. C. et al. The Betelgeuse Project: constraints from rotation. *Mon. Not. R. Astron. Soc.* **465**, 2654–2661 (2017).
59. Luo, T., Umeda, H., Yoshida, T. & Takahashi, K. Stellar models of Betelgeuse constrained using observed surface conditions. *Astrophys. J.* **927**, 115 (2022).
60. Davies, B. et al. The temperatures of red supergiants. *Astrophys. J.* **767**, 3 (2013).
61. Začs, L. & Puķītis, K. Evidence of increased macroturbulence for Betelgeuse during Great Dimming. *Res. Not. Am. Astron. Soc.* **5**, 8 (2021).
62. Alexeeva, S. et al. Spectroscopic evidence for a large spot on the dimming Betelgeuse. *Nat. Commun.* **12**, 4719 (2021).
63. López Ariste, A. et al. Three-dimensional imaging of convective cells in the photosphere of Betelgeuse. *Astron. Astrophys.* **661**, A91 (2022).
64. Aronson, H., Baumgarte, T. W. & Shapiro, S. L. Did a close tidal encounter cause the Great Dimming of Betelgeuse? Preprint at <https://arxiv.org/abs/2201.08438> (2022).
65. Chiavassa, A. et al. Radiative hydrodynamics simulations of red supergiant stars. II. Simulations of convection on Betelgeuse match interferometric observations. *Astron. Astrophys.* **515**, A12 (2010).
66. Granzer, T., Weber, M., Strassmeier, K. G. & Dupree, A. The curious case of Betelgeuse. In *The 20.5th Cambridge Workshop on Cool Stars, Stellar Systems, and the Sun* (CS20.5) 41 (2021). <https://doi.org/10.5281/zenodo.4561732>
67. Heger, A., Jeannin, L., Langer, N. & Baraffe, I. Pulsations in red supergiants with high L/M ratio. Implications for the stellar and circumstellar structure of supernova progenitors. *Astron. Astrophys.* **327**, 224–230 (1997).
68. Wasatonic, R. P., Guinan, E. F. & Durbin, A. J. V-band, near-IR, and TiO photometry of the semi-regular red supergiant TV Geminorum: long-term quasi-periodic changes in temperature, radius, and luminosity. *Publ. Astron. Soc. Pac.* **127**, 1010 (2015).
69. Ivezić, Z., Nenkova, M. & Elitzur, M. User manual for DUSTY. Preprint at <https://arxiv.org/abs/astro-ph/9910475> (1999).
70. Beasor, E. R. & Davies, B. The evolution of red supergiants to supernova in NGC 2100. *Mon. Not. R. Astron. Soc.* **463**, 1269–1283 (2016).
71. Ossenkopf, V., Henning, T. & Mathis, J. S. Constraints on cosmic silicates. *Astron. Astrophys.* **261**, 567–578 (1992).
72. Okuyama, A. et al. Validation of Himawari-8/AHI radiometric calibration based on two years of in-orbit data. *J. Meteorol. Soc. Jpn* **96B**, 91–109 (2018).
73. Ljung, G. M. & Box, G. E. On a measure of lack of fit in time series models. *Biometrika* **65**, 297–303 (1978).
74. Wenger, M. et al. The SIMBAD astronomical database. The CDS reference database for astronomical objects. *Astron. Astrophys. Suppl. Ser.* **143**, 9–22 (2000).

Acknowledgements

We thank N. Matsunaga, T. Kamizuka, K. Tachibana, T. Onaka, N. Kobayashi, M. Jian and M. Ando for comments and discussion. We also thank the Meteorological Satellite Center of the Japan Meteorological Agency for explanations of the details of the Himawari-8 observations, in response to our inquiries. This work has been supported by the Masason Foundation. D.T., K.Y. and S.U. are financially supported by JSPS Research Fellowship for Young Scientists and accompanying Grants-in-Aid for JSPS Fellows (21J11555, 21J11266 and 21J20742, respectively). D.T. also acknowledges financial support from the Masason Foundation since 2018, from The University of Tokyo Toyota-Dwango Scholarship for Advanced AI Talents in 2020–21 and from Iwadare Scholarship Foundation in 2020. S.U. is supported by the WINGS-FoPM programme of the University of Tokyo. This study used the Himawari data downloaded from the Data Integration and Analysis System by the University of Tokyo. This study also used the variable-star observations from the AAVSO International Database contributed by observers worldwide. Data analysis was in part carried out on the Multi-wavelength Data Analysis System operated by the Astronomy Data Center of the National Astronomical Observatory of Japan, and in a computer environment funded by JSPS KAKENHI (JP25287119 and 20H05731).

Author contributions

D.T. and S.U. initiated this work. D.T. analysed the photometric datasets. K.Y. led the photometry of the Himawari-8 images, and D.T. and S.U. partly contributed to it. All the authors contributed substantially to the discussion and the writing.

Competing interests

The authors declare no competing interests.

Additional information

Extended data is available for this paper at <https://doi.org/10.1038/s41550-022-01680-5>.

Supplementary information The online version contains supplementary material available at <https://doi.org/10.1038/s41550-022-01680-5>.

Correspondence and requests for materials should be addressed to Daisuke Taniguchi.

Peer review information *Nature Astronomy* thanks Robert Gehr and the other, anonymous, reviewer(s) for their contribution to the peer review of this work.

Reprints and permissions information is available at www.nature.com/reprints.

Publisher's note Springer Nature remains neutral with regard to jurisdictional claims in published maps and institutional affiliations.



Open Access This article is licensed under a Creative Commons Attribution 4.0 International License, which permits use, sharing, adaptation, distribution and reproduction in any medium or format, as long as you give appropriate credit to the original author(s) and the source, provide a link to the Creative Commons license, and indicate if changes were made. The images or other third party material in this article are included in the article's Creative Commons license, unless indicated otherwise in a credit line to the material. If material is not included in the article's Creative Commons license and your intended use is not permitted by statutory regulation or exceeds the permitted use, you will need to obtain permission directly from the copyright holder. To view a copy of this license, visit <http://creativecommons.org/licenses/by/4.0/>.

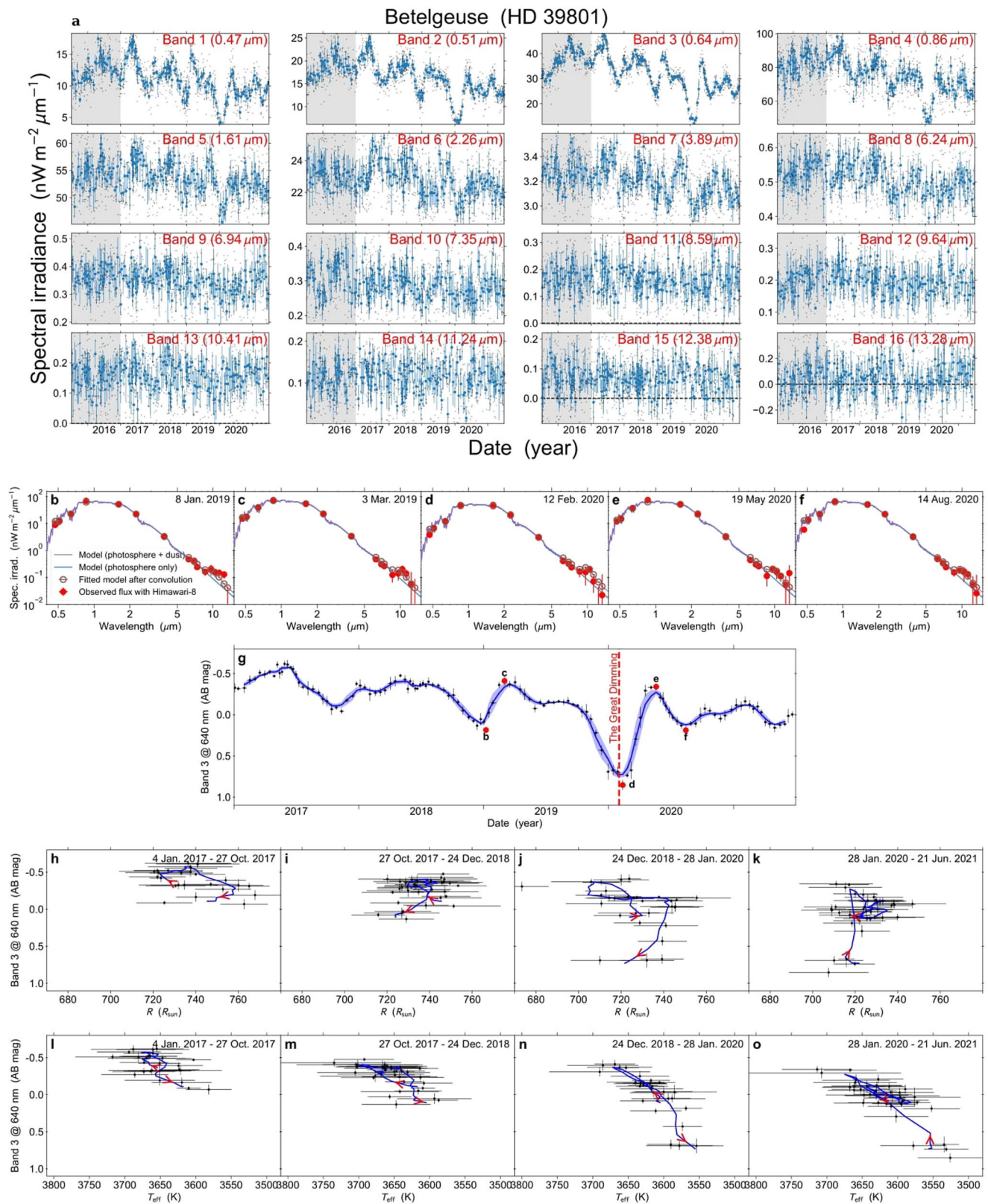
© The Author(s) 2022

Band No.	λ_0^a (μm)	$\Delta\lambda^a$ (μm)	Pixel scale		m_{AB}^c (mag)	F_{max}^d ($\text{nW m}^{-2} \mu\text{m}^{-1}$)	LSB ^e	z_{min}^f (km)	LB test p value ^g	
			(km) ^b	(arcsec)					Rigel	Procyon
1	0.471	0.041	1.0	5.76	2.4	597	0.38	75	0.419	0.509
2	0.510	0.031	1.0	5.76	2.5	560	0.35	75	0.174	0.210
3	0.639	0.082	0.5	2.88	2.4	121	0.31	75	0.003	0.321
4	0.857	0.034	1.0	5.76	0.8	288	0.182	60	0.884	0.859
5	1.610	0.041	2.0	11.53	0.7	287	0.045	65	0.341	0.204
6	2.257	0.044	2.0	11.53	0.9	89.1	0.0141	60	0.938	0.609
7	3.89	0.20	2.0	11.53	2.0	40.2	0.000 79	55	0.964	0.329
8	6.24	0.82	2.0	11.53	0.3	29.9	0.0048	90	0.331	0.836
9	6.94	0.40	2.0	11.53	−0.1	36.4	0.0058	100	0.288	0.396
10	7.35	0.19	2.0	11.53	−0.3	38.8	0.0031	100	0.893	0.382
11	8.59	0.37	2.0	11.53	−0.7	50.6	0.0040	100	0.270	0.500
12	9.64	0.38	2.0	11.53	−0.8	49.7	0.0039	130	0.689	0.316
13	10.41	0.42	2.0	11.53	−1.2	47.5	0.0038	90	0.756	0.870
14	11.24	0.67	2.0	11.53	−1.0	44.3	0.0035	80	0.913	0.250
15	12.38	0.97	2.0	11.53	−1.4	39.4	0.0031	100	0.658	0.285
16	13.28	0.56	2.0	11.53	−2.5	36.0	0.0058	100	0.351	0.074

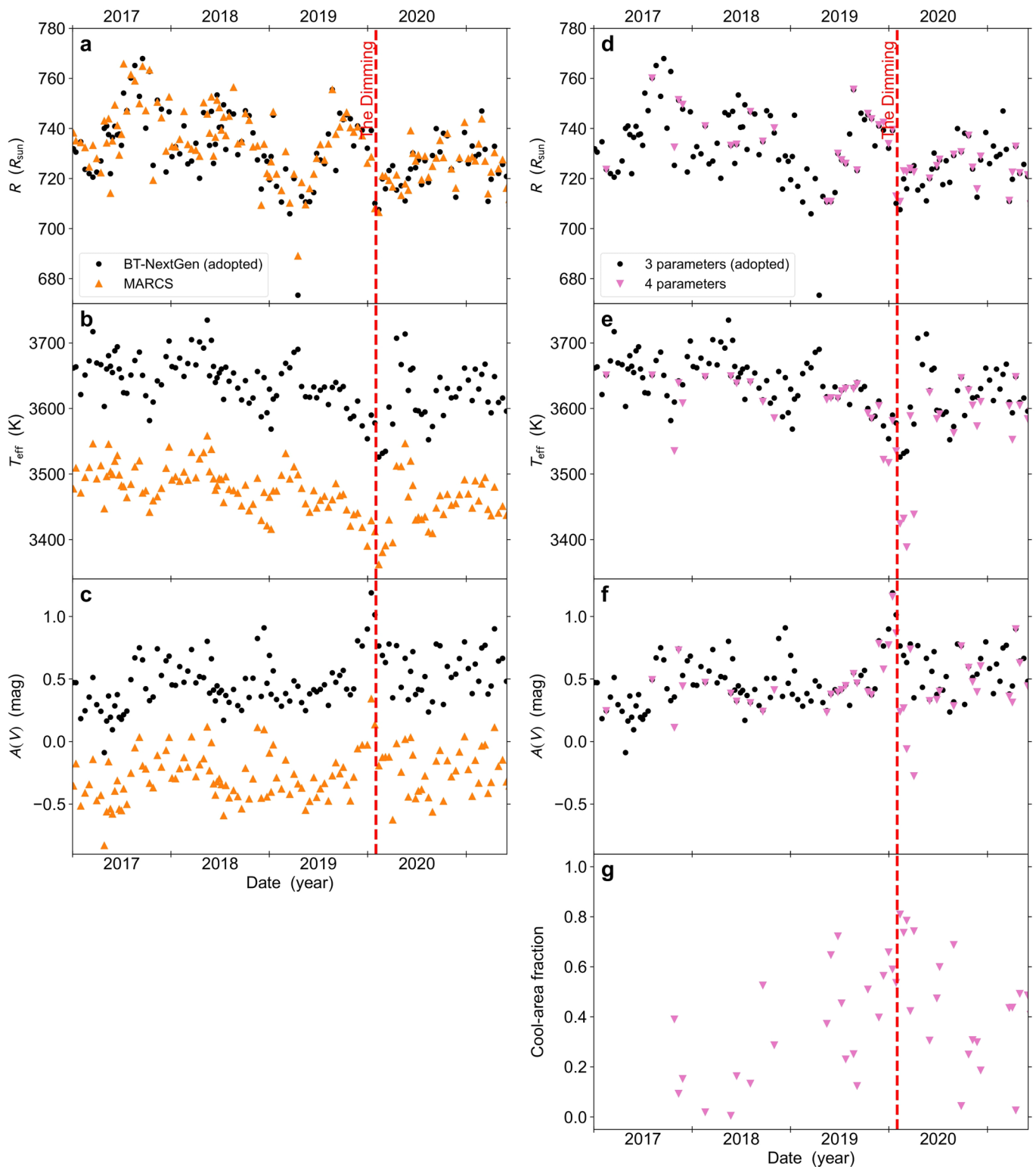
Extended Data Fig. 1 | Basic properties of the Himawari-8 AHI images and the thresholds used for photometry. ^aEach band is centered on λ_0 and has the FWHM $\Delta\lambda$; ^bSpatial resolution at the sub-satellite point, i.e., 35,786 km from the satellite; ^cSky- 3σ limiting AB magnitude for each band at the declination of Betelgeuse; ^dMaximum valid flux per pixel in the calibrated L1B file format of Himawari-8 images. According to results of ground tests⁷², the saturation flux of the AHI itself is larger than these values; ^eLeast significant bit (LSB) of L1B images; i.e. the flux of each pixel is measured in increments of LSB; ^fMinimum distance between the Betelgeuse line of sight and the edge of the Earth's edge accepted for photometric analyses in this study; ^g p value of Ljung-Box test⁷³, with the time delays up to 30 days for the two non-variable stars, Rigel and Procyon.

Name	HD number	Sp. Type ^a	Dec. ^a (deg)	Frequency ^b (days ⁻¹)
Betelgeuse	39801	M1–M2Ia–Iab	+7.41	0.58
Rigel	34085	B8Iae	–8.20	0.91
Procyon	61421	F5IV–V+DQZ	+5.22	0.33
δ Oph	146051	M0.5III	–3.69	0.29
α Cet	18884	M1.5IIIa	+4.09	0.48

Extended Data Fig. 2 | The stars for which we performed photometry. ^aSpectral type and declination (J2000.0) taken from the SIMBAD database⁷⁴ on 15 June 2021; ^bTypical frequency at which the star appear in the Himawari-8 images.



Extended Data Fig. 3 | Results of the photometry and the SED fitting for Betelgeuse. **a**, Light curves of Betelgeuse in all bands. The black dots represent individual measurements, and the blue circles and vertical bars represent the medians and standard errors after binning, respectively. The photometric measurements in the gray-shaded areas, that is, in 2015 and 2016, were not used in the analysis. **b-f**, Five results of the SED fitting as examples, whose observation epoch are shown in **g**. The red and brown circles represent the observed and fitted spectral irradiances for each band, respectively. The purple and blue lines represent the fitted spectrum before the convolution with the response function. **g**, The light curve of Betelgeuse at Band 3 in AB magnitudes, as in Fig. 2. **h-k** and **l-o**, The relation between the radius R or effective temperature T_{eff} , respectively, and Band 3 magnitude with the smoothed trajectory created by averaging five points.



Extended Data Fig. 4 | Comparison of the results of SED fitting with different model assumptions. In all the panels, the black circles indicate the results adopted in this paper (the same as Fig. 2), which use the grid of Next-Gen model spectra⁴⁹, assuming three free parameters in the fitting. **a-c**, The effect of the adopted model-spectrum grid: Next-Gen⁴⁹ (blue circles) vs. MARCS⁵⁵ (upward-pointing orange triangles). **d-g**, The effect of the number of parameters: three parameters (blue circles) vs. four parameters (downward-pointing pink triangles).